



HAL
open science

Interaction of an atmospheric pressure plasma jet with grounded and floating metallic targets: simulations and experiments

Pedro Viegas, Marlous Hofmans, Olivier van Rooij, Adam Obrusník, Bart L M Klarenaar, Zdenek Bonaventura, Olivier Guaitella, Ana Sobota, Anne Bourdon

► To cite this version:

Pedro Viegas, Marlous Hofmans, Olivier van Rooij, Adam Obrusník, Bart L M Klarenaar, et al.. Interaction of an atmospheric pressure plasma jet with grounded and floating metallic targets: simulations and experiments. *Plasma Sources Science and Technology*, 2020, 29 (9), pp.095011. 10.1088/1361-6595/aba7ec . hal-02960641

HAL Id: hal-02960641

<https://hal.science/hal-02960641>

Submitted on 12 Oct 2020

HAL is a multi-disciplinary open access archive for the deposit and dissemination of scientific research documents, whether they are published or not. The documents may come from teaching and research institutions in France or abroad, or from public or private research centers.

L'archive ouverte pluridisciplinaire **HAL**, est destinée au dépôt et à la diffusion de documents scientifiques de niveau recherche, publiés ou non, émanant des établissements d'enseignement et de recherche français ou étrangers, des laboratoires publics ou privés.

PAPER • OPEN ACCESS

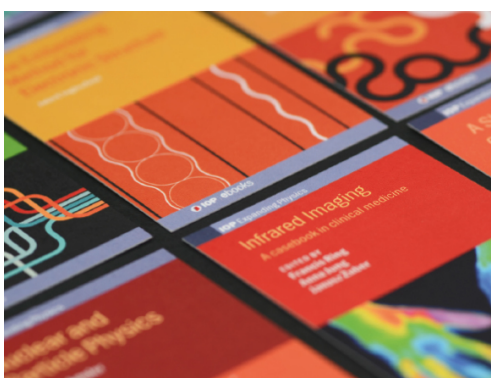
Interaction of an atmospheric pressure plasma jet with grounded and floating metallic targets: simulations and experiments

Recent citations

- [Ion energies delivered by negative and positive ionization waves to flat dielectric surfaces](#)
Natalia Yu Babaeva and George V Naidis

To cite this article: Pedro Viegas *et al* 2020 *Plasma Sources Sci. Technol.* **29** 095011

View the [article online](#) for updates and enhancements.





IOP | ebooks™

Bringing together innovative digital publishing with leading authors from the global scientific community.

Start exploring the collection—download the first chapter of every title for free.

Interaction of an atmospheric pressure plasma jet with grounded and floating metallic targets: simulations and experiments

Pedro Viegas^{1,4,5} , Marlous Hofmans^{1,2} , Olivier van Rooij², Adam Obrusnik³ , Bart L M Klarenaar² , Zdenek Bonaventura³ , Olivier Guaitella¹ , Ana Sobota²  and Anne Bourdon¹ 

¹ LPP, CNRS, École Polytechnique, Sorbonne Université, Université Paris-Saclay, IP-Paris, 91128 Palaiseau, France

² Department of Applied Physics, EPG, Eindhoven University of Technology, The Netherlands

³ Department of Physical Electronics, Faculty of Science, Masaryk University, Brno, Czech Republic

E-mail: p.viegas@diffier.nl, marlous.hofmans@lpp.polytechnique.fr, a.sobota@tue.nl and anne.bourdon@lpp.polytechnique.fr

Received 5 April 2020, revised 29 June 2020

Accepted for publication 21 July 2020

Published 14 September 2020



Abstract

The interaction of kHz μ s-pulsed atmospheric pressure He jets with metallic targets is studied through simulations and experiments, focusing on the differences between floating and grounded targets. It is shown that the electric potential of the floating target is close to grounded in the instants after the impact of the discharge, but rises to a high voltage, potentially more than half of the applied voltage, at the end of the 1 μ s pulse. As a result, a return stroke takes place after the discharge impact with both grounded and floating targets, as a redistribution between the high voltage electrode and the low voltage target. Electric field, electron temperature and electron density in the plasma plume are higher during the pulse with grounded target than with floating target, as gradients of electric potential progressively dissipate in the latter case. Finally, at the fall of the pulse, another electrical redistribution takes place, with higher intensity with the highly-charged floating target than with the grounded target. It is shown that this phenomenon can lead to an increase in electric field, electron temperature and electron density in the plume with floating target.

Keywords: plasma jet, plasma-surface, metallic surfaces, floating, grounded, benchmarking


(Some figures may appear in colour only in the online journal)

1. Introduction

The interactions between non-thermal plasmas at intermediate to high pressures and surfaces is of great interest due to

⁴ Present address: DIFFER-Dutch Institute for Fundamental Energy Research, 5612 AJ Eindhoven, The Netherlands.

⁵ Author to whom any correspondence should be addressed.

 Original content from this work may be used under the terms of the [Creative Commons Attribution 4.0 licence](https://creativecommons.org/licenses/by/4.0/). Any further distribution of this work must maintain attribution to the author(s) and the title of the work, journal citation and DOI.

an increasing number of applications. These include biomedical treatment (Fridman *et al* 2008, Kong *et al* 2009, Graves 2014, Weltmann and von Woedtke 2017), surface modification (Noeske *et al* 2004, Cheng *et al* 2006, Fanelli and Fracassi 2017), catalysis (Guaitella *et al* 2006, Neyts 2016), and nitrification of liquids (Lindsay *et al* 2014). Plasma jets are very useful tools for the study of those interactions, as they are able to repetitively deliver in remote locations a wide range of reactive and charged species, high electric fields and UV photons, at atmospheric pressure and while keeping low gas temperature.

Thus, they are very promising devices for applications in the areas of material science, biomedicine (Collet *et al* 2014, Laroussi 2015) and agriculture (Ito *et al* 2018). Plasma jets have attracted a lot of attention in the past 20 years and are generally described in several reviews (Schutze *et al* 1998, Laimer and Stori 2007, Laroussi and Akan 2007, Lu *et al* 2012, 2014, Winter *et al* 2015, Reuter *et al* 2018).

Several works have studied interactions of jets with targets, finding not only that the plasma affects the surface, but also that discharge dynamics can vary dramatically when interacting with surfaces with different electrical properties (Sakiyama *et al* 2008, Bornholdt *et al* 2010, Urabe *et al* 2010). As such, in the last years there have been several investigations of jet interactions with targets of different electrical character: dielectric at floating electric potential (Sobota *et al* 2013, Wild *et al* 2014, Guaitella and Sobota 2015, Slikboer *et al* 2016, 2017, Liu *et al* 2017, Koné *et al* 2017, Slikboer *et al* 2018a, 2018b, Ji *et al* 2018, Klarenaar *et al* 2018a, Lazarou *et al* 2018) (Viegas *et al* 2018b, Hofmans and Sobota 2019, Sobota *et al* 2019, Slikboer *et al* 2019, Viegas and Bourdon 2020, Babaeva *et al* 2019, Wang *et al* 2019); dielectric attached to a grounded plate (Hofmann *et al* 2014, Breden and Raja 2014, Boselli *et al* 2014, Guaitella and Sobota 2015, Norberg *et al* 2015, Wang *et al* 2016, Yan and Economou 2016) (Ji *et al* 2018, Yue *et al* 2018, Schweigert *et al* 2019b, Simoncelli *et al* 2019, Viegas and Bourdon 2020); conductive at floating potential (Ito *et al* 2010, Robert *et al* 2015, Koné *et al* 2017, Ji *et al* 2018, Klarenaar *et al* 2018a, Hofmans and Sobota 2019, Schweigert *et al* 2019a, Babaeva *et al* 2019, Martinez *et al* 2019); conductive grounded (Hofmann *et al* 2014, Boselli *et al* 2014, Robert *et al* 2015, Norberg *et al* 2015, Yan and Economou 2016, Darny *et al* 2017) (Viegas *et al* 2018a, Ji *et al* 2018, Yue *et al* 2018, Schweigert *et al* 2019b, 2019a, Babaeva *et al* 2019, Wang *et al* 2019, Simoncelli *et al* 2019, Martinez *et al* 2019).

These studies have distinguished the effect of dielectric targets of different relative permittivities ϵ_r and conductivities and of metallic targets on discharge dynamics. With low values of ϵ_r (approximately $\epsilon_r \leq 20$) and conductivity and low capacitance, after the impact of the discharge on the target, the surface of the target is charged locally in a short time, which quickly leads to the depletion of the axial component of electric field and the rise of the radial component that sustains the propagation of the discharge on the surface (Norberg *et al* 2015, Yan and Economou 2016, Wang *et al* 2016, Yue *et al* 2018, Klarenaar *et al* 2018a, Viegas and Bourdon 2020). With high values of ϵ_r or conductivity (liquid water-based surfaces) and with metallic targets, the charging of the surface is slower or inexistent, there is no radial component of electric field and no discharge propagation on the surface. Instead, a higher voltage drop remains in the gap, which promotes a return stroke and the formation of a conductive channel (Loeb 1965, Sigmond 1984, Raizer 1991, Norberg *et al* 2015, Yan and Economou 2016, Darny *et al* 2017, Viegas *et al* 2018a, Yue *et al* 2018, Klarenaar *et al* 2018a, Hofmans and Sobota 2019, Babaeva *et al* 2019). The return stroke is an ionization wave that propagates with reverse polarity with respect to the first ionization front (Loeb 1965, Sigmond 1984, Darny *et al* 2017). It starts at the target where electron emission takes place

and propagates in an already ionized channel towards the powered electrode, provoking charge separation of opposite sign to that generated by the first wave, thus partially neutralizing the plasma channel (Raizer 1991, Viegas 2018). The return stroke is driven by the gradient of electric potential between the target and the powered electrode.

Despite some recent studies, the difference between grounded and floating conductive targets is less characterized. It has been reported by experiments that the He flow channeling in jets is stronger over grounded metallic targets than over those at floating potential (Robert *et al* 2015). Moreover, in Ji *et al* (2018), experiments and simulations of He jets have been used to compare the discharge dynamics with floating and grounded dielectric and metallic targets, obtaining higher velocities of propagation, maximum electric fields, higher species production and higher *E. coli* cell inactivation with the grounded targets. The faster discharge propagation towards grounded targets has also been observed in Ji *et al* (2018), Babaeva *et al* (2019), Viegas and Bourdon (2020), Martinez *et al* (2019). The simulation results in Babaeva *et al* (2019) have also shown higher ionization source term during propagation and higher electric field and electron density after impact on a conductive grounded target than on a conductive floating target. The experiments in Yue *et al* (2018), Schweigert *et al* (2019a) have also observed higher production of reactive species in jets interacting with grounded conductive targets than in jets interacting with dielectric or floating conductive targets. Schweigert *et al* (2019a) have reported lower viability of cancer cells when using a grounded substrate under the cells during plasma jet treatment. Furthermore, it has been shown through simulations in Viegas and Bourdon (2020) that a dielectric target attached to a ground is significantly more charged by a He jet than the same target at floating potential. These differences suggest the importance of grounding or not the target for applications.

Another subject not fully understood in jet-target interaction is the discharge dynamics at the fall of the applied voltage. In jet experiments with dielectric targets using AC voltages a faint back discharge has been reported at the reversion of applied voltage polarity (Sobota *et al* 2013, Slikboer *et al* 2016). In pulsed jets, similar phenomena have been reported at the fall of the pulse. In Norberg *et al* (2015) the dynamics of charges at the fall of the voltage pulse has been described through simulations, not as a new discharge but as a balance between remaining positive and negative charges in the plasma and on the target surface. In Yan and Economou (2016) simulations of jets with grounded dielectric and conductive targets have observed an electric field reversal and a brief heating of electrons at the fall of the applied voltage. In the free jet experiments in Lu *et al* (2017) a secondary discharge has been observed at the end of the pulse and it has been attributed to the residual charges left from the first discharge. It has been found to have opposite polarity with respect to the first discharge and to be associated to an electric field below 6 kV cm^{-1} . Moreover, in Yue *et al* (2018), Klarenaar *et al* (2018a) a faint discharge at the fall of the voltage pulse has been reported, observed in the whole plasma channel, more pronounced with metallic target at floating potential than

with dielectric or grounded metallic targets. The faint glow has been attributed to the neutralization of the space charge in the plasma channel in Yue *et al* (2018). In fact, in Kim *et al* (2018) the electric field reversal at the falling edge of a positive voltage pulse and consequent secondary ionization have been investigated with a full kinetic treatment in argon discharges between planar electrodes on nanosecond time scales. It is claimed that the secondary ionization is induced by charge transport in the bulk plasma region. In our previous works on pulsed jets with dielectric targets (Viegas *et al* 2018b, Slikboer *et al* 2019), we have shown through comparisons between experiments and simulations on the electric field in the target induced by surface charges that the electrical redistribution at the fall of the pulse neutralizes the positive charge on the target surface and in some cases charges the target negatively.

In our last work (Hofmans *et al* 2020) we have characterized a kHz atmospheric pressure He plasma jet without target powered by pulses of positive applied voltage through quantitative comparisons on several key parameters of plasma jet dynamics (i.e. length and velocity of discharge propagation, gas mixture composition, electron temperature and density and peak electric field) between experimental measurements combining different diagnostic techniques and two-dimensional numerical results. Excellent agreement has been obtained between experiments and simulations on the length and velocity of discharge propagation, the gas mixture distribution and the peak electric field in the discharge front, as well as a qualitative agreement on the electron density and temperature measured behind the high field front. Moreover, we have shown how the fall of the pulse of applied voltage leads to lowering the electric potential in the plasma and, in the case of short pulses, to stopping discharge propagation. In this paper we combine different experimental diagnostic techniques (imaging, Stark polarization spectroscopy peak electric field measurements, Thomson scattering measurements of electron properties in the plasma plume and high-voltage probe measurements of the temporal evolution of electric potential of the floating target) and 2D fluid simulations to study the interaction of a positive pulsed He plasma jet with metallic targets and the influence of grounding or not the target on discharge dynamics before the impact, after the impact and after the end of the pulse. Moreover, we compare discharge parameters with metallic targets with those from the jets in Hofmans *et al* (2020) without target.

Firstly, both the experimental and numerical setups for free jet, jet with metallic target at floating potential and jet with grounded metallic target are described in section 2. A set of assumptions to describe the floating metallic target in the model is proposed. Then, section 3.1 describes the general discharge dynamics with the three jet configurations in both experiments and simulations, focusing on discharge propagation and the associated peak electric field. Finally, section 3.2 describes in detail the charging of the floating metallic target and shows the influence it has on plasma parameters after the impact of the discharge on the target and after the fall of the pulse. As a result, the electrical redistribution associated

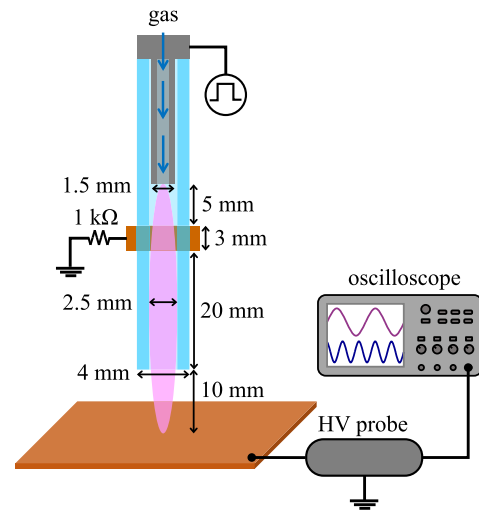


Figure 1. Schematic overview of the discharge setup used in the experiments when measuring the potential on the floating target.

to the fall of the pulse and its dependence on the target are characterized.

2. Setup

2.1. Experimental setup

The plasma jet used in the experiments consists of a pyrex tube with a stainless steel tube inside as powered electrode and a grounded copper ring on the outside. Helium flows through the inner electrode with a flux of 1.5 slm. All piping in the setup is made of stainless steel to limit impurities in the gas flow. In figure 1, the dimensions of the jet are shown. This jet has the same geometry as the jet used in Sobota *et al* (2016), Viegas *et al* (2018b), Slikboer *et al* (2019), Hofmans *et al* (2020) and is operated vertically downwards. The jet is powered by positive square high voltage pulses at a repetition rate of 5 kHz. The width t_f and amplitude V_P of the pulses are varied to be 1 or 10 μ s and 4, 5 or 6 kV, respectively. A function generator (Agilent 33220A) and high voltage power supply (Spellman UHR10P60/CL/220) couple, respectively, the pulse shape and the DC high voltage to a high voltage pulse generator (DEI PVX-4110) that supplies the high voltage pulses to the inner electrode of the jet. Three jet configurations are used: free jet, jet with metallic target at floating potential and jet with grounded metallic target.

As target, a copper plate of 8 mm \times 8 mm with a thickness of 1 mm is used. For the measurements with target, the target is placed on a plastic, insulated plate that is connected to the holder of the jet itself. The distance between the target and the nozzle of the jet is set to 1 cm. In general, the distance between the target and the closest grounded plane, which is a table, is around 30 cm. The target can be grounded by connecting a cable to the ground on one end and to the target on the other end.

As in Hofmans *et al* (2020), the voltage and current that are applied to the jet are measured at the inner ring by a high voltage probe (LeCroy PHV4-3432) and a Rogowski coil (Peason Current Monitor 6585), respectively. The current measured

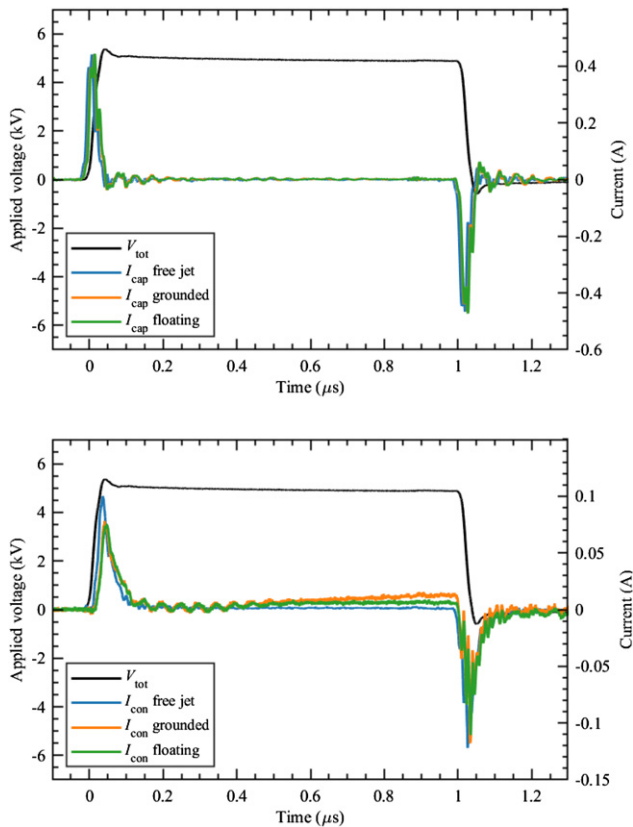


Figure 2. Applied voltage pulse together with the capacitive current (on top) and the conductive current (on bottom) for the free jet, grounded target and floating target cases. The y-axis for the conductive current has a smaller scale than for the capacitive current for better visibility.

with both the helium flow and the applied voltage, in the presence of the plasma, corresponds to the total current I_{tot} , while the current measured only with the applied voltage, without plasma and helium flow, corresponds to the capacitive current I_{cap} . This capacitive current arises from the circuit of the plasma equipment, which behaves as a capacitor. Subtracting the capacitive current from the total current yields the conductive current I_{con} , which is the current that flows through the plasma acting as a conductor. Figure 2 shows the applied voltage as function of time, as well as the capacitive current I_{cap} in the top figure and the conductive current I_{con} in the bottom figure, for the three jet configurations: free jet, jet with floating metallic target and jet with grounded metallic target. I_{tot} is not represented for conciseness, but it can be found by adding I_{con} to I_{cap} . It can be seen that the capacitive current is basically the same in the three cases, as expected, but a difference is visible at the conductive current, namely just before the negative current peak. The implications of these differences will be analysed in section 3.2.

The behavior of the plasma jet in the different cases (free jet, floating and grounded target) is studied by imaging with an ICCD camera (Stanford Computer Optics 4Picosec S20Q). From these images, the position and velocity of the ionization front along the axis of the jet are determined.

To determine the electric field in the ionization front of the jet, the Stark polarization spectroscopy setup of Hofmans and

Sobota (2019) is used as in Hofmans *et al* (2020). The He I 492.2 nm line is studied to determine the electric field from the peak-to-peak wavelength difference between the allowed and the forbidden component of the line, according to the calibration in Hofmans and Sobota (2019). Scanning the jet inside the tube and outside in the effluent yields the axial profile of the electric field at the center of the jet. Measurements of electric field are performed for the free jet and for the jet interacting with a floating as well as a grounded metallic target.

The same Thomson scattering setup as in Klarenaar *et al* (2018a), Hofmans *et al* (2020) is used to measure the electron density and temperature in the plasma jet when interacting with a floating metallic target. The jet is positioned in such a way that the focus of the 532 nm laser beam lies in the center of the jet at 8.7 mm from the tube exit, thus at 1.3 mm above the target, which is the closest distance to the target possible without the laser interacting with the target. Then, the electron density and temperature are probed as a function of time. The laser operates at 100 Hz with 140 mJ per pulse and at the focal point each laser pulse has a width of 100 μm and a duration of 10 ns. This means that all scattered light within a cylindrical volume of approximately $7.9 \times 10^{-4} \text{ mm}^3$ and during 10 ns is captured. A volume Bragg grating is used to filter out the Rayleigh stray light from the Thomson signal (Klarenaar *et al* 2015). More details about this setup can be found in Klarenaar *et al* (2015), (2018a), (2018b). As in our previous work (Hofmans *et al* 2020), we take the statistical spread as error instead of the error that results from the fit. By performing measurements on different days at the same settings and at a position of 8.7 mm from the tube exit, a spread of 20% in the values of n_e was found. This error is larger than the error resulting from the fit, which is only a few percent. Considering the uncertainties in the experiments as discussed in Hofmans *et al* (2020), among which the influence of the laser pulse on the plasma, we consider 20% as error for n_e and T_e more realistic.

To measure the potential on the floating metallic target as function of time, a high voltage probe (Tektronix P6015A 100 M Ω 3.0 pF) is connected to the target and the results are shown on an oscilloscope (LeCroy waveRunner 6100A 1 GHz [dual 10 GS/s, quad 5 GS/s]). This setup is shown schematically in figure 1.

2.2. Numerical setup

We use a two-dimensional axisymmetric fluid model described in our previous works (Slikboer *et al* 2019, Viegas and Bourdon 2020, Hofmans *et al* 2020). The numerical setup is shown in figure 3. The model assumes in the whole domain atmospheric pressure and room-temperature $T = 300 \text{ K}$. The geometries taken are as close as possible as in the experiments. A dielectric pyrex tube with a relative permittivity of $\epsilon_r = 4$, length 3.3 cm (between $z = 0.0 \text{ cm}$ and $z = -3.3 \text{ cm}$), internal radius $r_{\text{in}} = 1.25 \text{ mm}$ and outer radius $r_{\text{out}} = 2.0 \text{ mm}$ is used. Helium flows through the tube with a 1.5 slm flux as in the experimental conditions. A ring electrode is set inside the tube between $z = -2.8 \text{ cm}$ and $z = -3.3 \text{ cm}$ with inner radius 0.4 mm and outer radius 1.25 mm and a grounded ring is wrapped around the tube between $z = -2.0 \text{ cm}$ and $z = -2.3 \text{ cm}$. The inner ring is powered by a positive applied voltage that

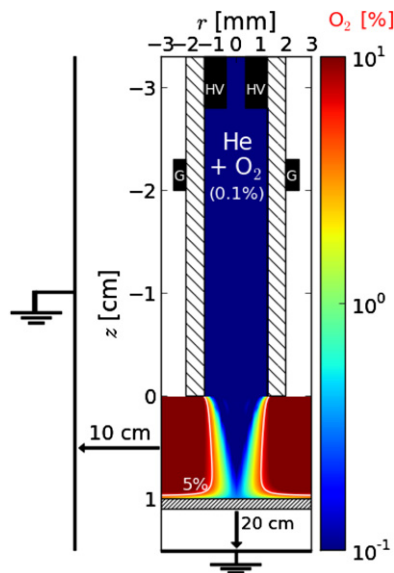


Figure 3. Side view schematics of the discharge setup used in the simulations in the case with metallic target at floating potential. The colour plot and the contour curves show the O_2 spatial distribution in the He– O_2 mixture (percentage over a total of $2.45 \times 10^{19} \text{ cm}^{-3}$ gas density).

increases from zero at $t_0 = 0$ ns during 50 ns until it reaches a plateau voltage V_p . It is then constant until $t = t_f$ and decreases until $t_f + 50$ ns, when it reaches zero, as in Hofmans *et al* (2020).

Three geometries are studied: (1) a free jet with no target present, but with a grounded plane set far from the tube at $z = 20$ cm. This is the same jet configuration as in Hofmans *et al* (2020); (2) a jet with conductive metallic target at floating potential placed at $z = 1$ cm with 1 mm thickness and $\sim 64 \text{ cm}^2$ surface (~ 4.5 cm radius) as in the experiments, with a grounded plane set at $z = 20$ cm. This is the case represented in figure 3; (3) a jet with conductive metallic target at grounded potential placed at $z = 1$ cm.

The metallic targets are modelled as in Viegas (2018), with infinite conductivity. To model the conductive target at a floating potential, we assume a very high relative permittivity $\epsilon_r = 1000$, which guarantees that the target is isopotential. Unlike the grounded metal, the floating target charges and uncharges through the interaction with the plasma. However, unlike the case with dielectric surfaces, we consider that charges are conducted instantaneously inside the metallic material. Thus, we integrate the fluxes of inwards- and outwards-directed charged particles in time, to obtain the total net charge in the target Q and we distribute this charge instantaneously and homogeneously in the target as net volume charge density ρ . This approach is similar to the one recently used in Babaeva *et al* (2019), describing a floating metal as a material with $\epsilon_r = 80$ and high conductivity. Finally, we consider the target as an ideal metal, i.e. a perfect absorber and perfect emitter, where an infinite number of free conducting charges can be exchanged with the plasma by mediation of the electric field. Therefore, we consider as for the grounded metallic target and the inner ring electrode, that electrons are emitted and

absorbed and that ions are neutralized following a Neumann boundary condition for their fluxes through electric drift.

Figure 3 shows that in the model, the discharge setup is placed inside a grounded cylinder with a radius of 10 cm, to clearly define boundary conditions. The discharge dynamics is simulated through drift–diffusion–reaction equations for mean electron energy, electrons, positive ions and negative ions, and reaction equations for neutral species, coupled with Poisson’s equation in cylindrical coordinates (z, r):

$$\frac{\partial}{\partial t}(n_e \epsilon_m) + \nabla \cdot \mathbf{j}_e = -|q_e| \mathbf{E} \cdot \mathbf{j}_e - \Theta_e \quad (1)$$

$$\mathbf{j}_e = -n_e \epsilon_m \mu_e \mathbf{E} - D_e \nabla(n_e \epsilon_m) \quad (2)$$

$$\frac{\partial n_i}{\partial t} + \nabla \cdot \mathbf{j}_i = S_i \quad (3)$$

$$\mathbf{j}_i = (q_i/|e|) n_i \mu_i \mathbf{E} - D_i \nabla n_i \quad (4)$$

$$\epsilon_0 \nabla \cdot (\epsilon_r \nabla V) = -\rho - \sigma \delta_s \quad (5)$$

$$\mathbf{E} = -\nabla V; \rho = \sum q_i n_i \quad (6)$$

where $n_e = n_e \epsilon_m$ is the electron energy density, defined as the product of the electron density with the mean electron energy, Θ_e represents the power lost by electrons in collisions and j_e is the flux of n_e by drift and diffusion. n_i, q_i, j_i, μ_i and D_i are the number density, charge, flux, mobility and diffusion coefficient of each species i , respectively. S_i is the rate of production and destruction of species i by kinetic processes and by photoionization. V is the electric potential, \mathbf{E} the electric field, e the electron charge, ϵ_0 the vacuum permittivity, ϵ_r the relative permittivity and δ_s the Kronecker delta (1 on the dielectric/gas interface). At the surface of the tube, secondary emission of electrons by ion bombardment ($\gamma = 0.1$ for all ions) is taken into account. The surface charge density σ on the surface of the dielectric is obtained by integrating in time charged particle fluxes through electric drift to the surface. We consider that these charges then remain immobile on the surface of the dielectric.

In the experiments there is a high repetition rate ($f = 5$ kHz). However, there is uncertainty on what the exact initial conditions should be to reproduce the repetitive discharges (Naidis 2011). To take this into account, we consider, as in our previous works (Viegas *et al* 2018a, 2018b, Slikboer *et al* 2019, Viegas and Bourdon 2020, Hofmans *et al* 2020), a standard uniform initial preionization density $n_{\text{init}} = 10^9 \text{ cm}^{-3}$ of electrons and O_2^+ . However, no initial surface charges are considered on the surfaces. As in our previous works, the static flow is precalculated using COMSOL (2016) (Arjunan *et al* 2016, Viegas 2018). In Hofmans *et al* (2020), the flow calculation from Sobota *et al* (2016) with 1.5 slm of helium with 1000 ppm of air impurities flowing through the tube into air has been used and compared with radially-resolved Raman scattering measurements of air density ($\text{N}_2 + \text{O}_2$) in free jet configuration, yielding a good agreement. In this work, we use the same flow calculation for the free jet. For the cases with target, we use the same model to recalculate the flow for the geometry in figures 1 and 3 with a flow rate of 1.5 slm. Then, to use

the local gas mixture compositions in the plasma model, we consider that helium contains O_2 impurities and flows downstream into an O_2 environment, as an approximation to air, as in Hofmans *et al* (2020). The spatial distribution of O_2 in the He– O_2 mixture obtained from the flow calculation with target is presented in figure 3.

The reaction scheme proposed in Viegas and Bourdon (2020) is used to describe the kinetics in the He– O_2 plasma, including a total of 55 reactions with 10 species. All the parameters related to electron kinetics are calculated with the electron Boltzmann equation solver BOLSIG+ Hagelaar and Pitchford (2005), using the IST-Lisbon database of cross sections in LXCat Pancheshnyi *et al* (2012), IST (2018), as functions of both the local gas mixture and the local mean electron energy ϵ_m . We describe photoionization using the approach described in Bourdon *et al* (2016), Slikboer *et al* (2019). The ionizing radiation is assumed to be proportional to the excitation rate of helium atoms by electron impact and the photoionization source term is taken as proportional to the amount of O_2 (X_{O_2}) and thus we use as photoionization proportionality coefficient $A_{ph} = 100 \times X_{O_2}$ (Bourdon *et al* 2016).

A finite volume approach and a Cartesian mesh are used in the model. The mesh size is $10 \mu\text{m}$, axially between $z = -3.3 \text{ cm}$ and $z = 5.0 \text{ cm}$ (free jet case) or $z = 1.1 \text{ cm}$ (floating target case) or $z = 1.0 \text{ cm}$ (grounded target case) and radially between $r = 0$ and $r = 3.0 \text{ mm}$. Then, in the rest of the domain the mesh size is expanded using a geometric progression. The average computational time required for a $2 \mu\text{s}$ simulation run to obtain the results presented in this paper was of four days with 64 MPI processes on a multicore cluster ‘Hopper’ (32 nodes DELL C6200 bi-pro with two 8-core processors, 64 GB of memory and 2.6 GHz frequency per node). Further details on the numerical schemes and other characteristics of the simulations are given in Viegas (2018).

3. Results and discussion

3.1. Characterization of discharge propagation and peak electric field

In this section, $V_p = 5 \text{ kV}$ and $t_f = 1 \mu\text{s}$ are used. Firstly, we compare discharge propagation with metallic targets at floating potential and at grounded potential. Figure 4 presents the experimental imaging from light emission in the two cases at different instants: during discharge propagation, at discharge impact on the target, before the fall of the pulse at $t_f = 1000 \text{ ns}$ and after the fall of the pulse. These emission images are wavelength integrated and show mostly emission in the range of 200–600 nm, since the sensitivity of the camera drops exponentially outside this wavelength range. From the emission spectra (not shown here) it is visible that the main sources are atomic helium (He I), the second positive system of N_2 and the first negative system of N_2^+ .

Figure 4 shows a similar propagation towards the floating and grounded targets. However, the discharge propagates faster towards the grounded target, as impact takes place at around 300 ns after the start of the pulse, which is about 60 ns

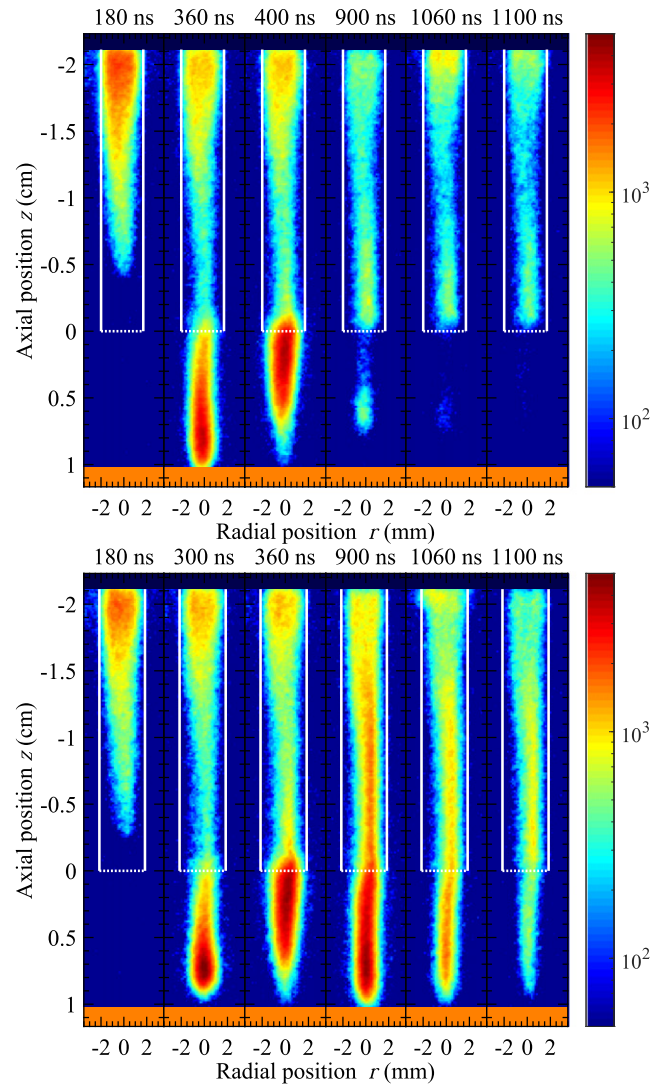


Figure 4. Imaging from the experiments with $V_p = 5 \text{ kV}$ and $t_f = 1 \mu\text{s}$, at different times, for the case with a metallic (copper) target at floating potential (on top) and with a grounded metallic target (on bottom). The colors represent the intensity of light emission in arbitrary units and are plotted on the same logarithmic scale in all images.

earlier than in the case with the target at floating potential. Then, both cases in figure 4 show a return stroke shortly after the impact on the target. In the grounded case, light emission from the plasma persists until the end of the pulse, and is particularly high in the plume region between the tube and the target, which suggests that reactivity in the plasma persists during that time. Conversely, with the target at floating potential, the emission intensity severely decreases until the end of the pulse in the whole plasma but especially in the plume. As the applied voltage falls to zero from 1000 to 1050 ns, the emission intensity progressively decreases in the whole plasma in the grounded case, while in the floating case it increases near the inner ring electrode from $t = 900$ to 1060 ns, which suggests an electric redistribution in that region. A light emission event at the end of the pulse has also been observed experimentally in Yue *et al* (2018), Klarenaar *et al* (2018a), Slikboer *et al* (2019) for jets with different targets. The results of

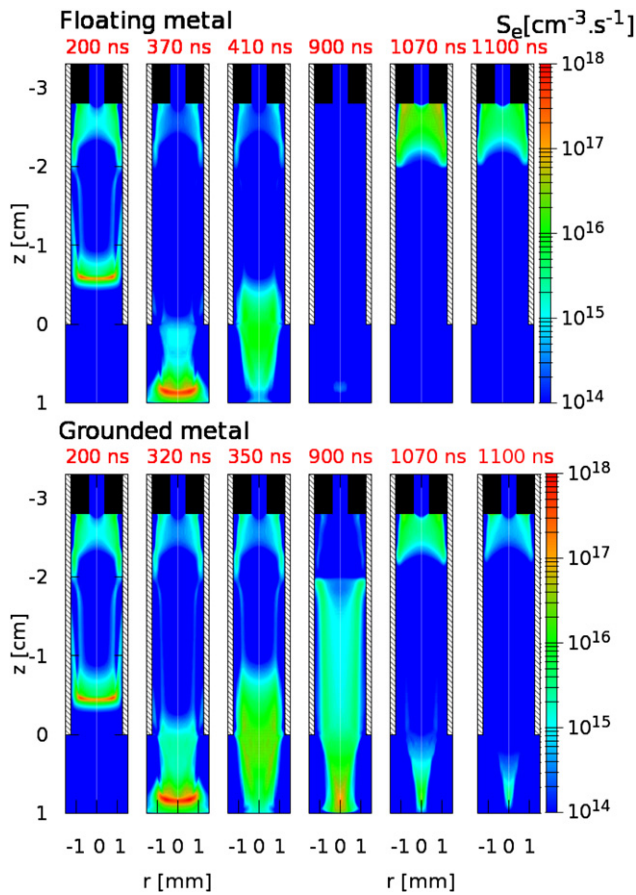


Figure 5. Cross section of the spatial distribution of the electron-impact ionization source term, from the simulations, with $V_P = 5$ kV and $t_f = 1$ μs at different times, for the case with a metallic target at floating potential (on top) and with a grounded metallic target (on bottom).

experimental imaging are compared to the simulation results shown in figure 5. This figure presents the spatial distribution of the electron-impact ionization rate S_e , driven by the electric field, for the same two cases as in figure 4 and also at different instants. In fact, the numerical electron-impact ionization source term and the experimental light emission can be qualitatively compared, as is common approach (Lietz *et al* 2019).

Figure 5 shows that in the simulations, as in the experiments, discharge propagation is faster towards the grounded target than towards the target at floating potential. The difference in time of impact between the two cases is approximately 50 ns, which is very close to the experimental one of 60 ns. For each case, the discharge impact on the target takes place around 10 to 20 ns later in the simulations than in the experiments. It has been shown in Hofmans *et al* (2020) that this difference is mostly due to the time of ignition of the discharge. The difference in ignition time is attributed to the uncertainty in memory effects, such as the possibility of leftover surface charges between pulses (repetition rate of 5 kHz) on the inner surface of the dielectric tube, that are not taken into account in the simulations containing only one pulse. Indeed, it has been shown in that work that the propagation velocity in a free jet is the same in experiments and simulations. With both targets,

the plasma structure is similar in the experiments and the simulations. However, close to the electrodes ($z \simeq -2$ cm), the plasma appears to be more centered in the experiments than in the simulations, in which case S_e has its maximum close to the tube walls. Conversely, close to the nozzle, it is shown that the discharge propagates with a wider structure in the experiments than in the simulations.

As in the experiments, figure 5 shows a return stroke after the impact with both the floating and grounded targets, with values of S_e around 10^{16} $\text{cm}^{-3}\cdot\text{s}^{-1}$ in the floating target case at $t = 410$ ns and up to 10^{17} $\text{cm}^{-3}\cdot\text{s}^{-1}$ with grounded target at $t = 350$ ns. The return stroke is driven by the gradient of electric potential between the target and the powered electrode that transports electrons emitted from the metallic targets, as will be shown in section 3.2. Its presence with the target at floating potential suggests that the target has a low potential immediately after the impact of the discharge. With the floating target, it is visible that S_e in the plasma in the simulations decreases from the time of impact to the end of the pulse. Indeed, S_e is no longer visible at $t = 900$ ns in the floating target case. Conversely, with the grounded target, S_e remains visible until the end of the pulse, with higher intensity in the plume than in the tube, with values up to 10^{17} $\text{cm}^{-3}\cdot\text{s}^{-1}$. Both results agree with the experimental observations in figure 4 and the simulation results in Babaeva *et al* (2019). These results imply that an electric field remains in the plasma between the powered electrode and the grounded target, while in the case of the target at floating potential the potential gradients in the plasma dissipate as the target is charged, as will be shown in section 3.2.

After the end of the pulse, as the voltage of the inner ring electrode falls to zero, a new dynamics takes place. Indeed, as happens with light emission from experiments, S_e increases close to the inner electrode, which requires the presence of an electric field in that region, between the grounded inner ring and the plasma. S_e after the fall of the pulse is more intense with the charged target at floating potential, reaching 10^{17} $\text{cm}^{-3}\cdot\text{s}^{-1}$, than with the grounded target. During the pulse, as the floating target is charged, its electric potential can rise to values of the same order of the applied voltage, which is not the case with the grounded target, as will be shown in section 3.2. Then, when the applied voltage falls to zero, the gradient of potential between the new grounded electrode and the plasma is higher in the case with floating target than with grounded target.

In order to deepen the understanding on discharge propagation and quantitatively compare simulations and experiments, in figure 6 we follow the position of the discharge front in time in experiments and simulations. Besides the two cases presented in figures 4 and 5, the results with free jet (no target) and $V_P = 5$ kV are also shown and compared. In the experiments, the position of the discharge front is obtained from the maximum of the light emission intensity, with an errorbar of 0.07 cm, while in the simulations it is obtained from the maximum of the axial component of electric field $E_{z\text{MAX}}$. That approach allows to follow the propagation of the first ionization wave in both experiments and simulations and of the

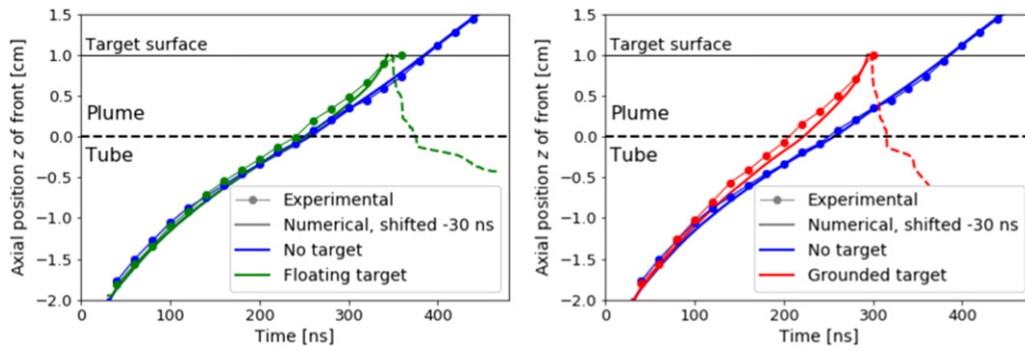


Figure 6. Temporal evolution of the position of the discharge front during propagation and after impact, from simulations and experiments, with $V_P = 5$ kV and for three different configurations. On the left, free jet (no target) and metallic target at floating potential. On the right, free jet and grounded target. The return stroke from the simulations is represented with dashed lines. The experimental errorbar is 0.07 cm.

return stroke in simulations but not in experiments. The numerical result is shifted by 30 ns to account for the difference in time of ignition with respect to the experiments.

Figure 6 shows, as in Hofmans *et al* (2020), a small difference between the ignition time in experiments and simulations of about 30 ns and an excellent agreement in discharge propagation for every case. In both experiments and simulations, the discharge propagating towards the grounded target is faster than in the other cases, all along the propagation, due to the proximity of the ground, as has also been shown in experiments and simulations in Ji *et al* (2018), Babaeva *et al* (2019), Viegas and Bourdon (2020), Martinez *et al* (2019). Conversely, the discharge propagates faster towards the floating target than in the free jet case only when the discharge is close to the target. The ground is placed at $z = 20$ cm in both cases and thus does not justify the difference. Indeed, the difference in velocity is due to the influence of ϵ_r on propagation ($\epsilon_r = 1000$ in the floating target case and $\epsilon_r = 1$ in air in the free jet case). It has been shown in Viegas and Bourdon (2020) that ϵ_r does not significantly change the velocity of discharge propagation, except when the discharge front is very close to the target surface, mostly in the last 5 mm of propagation. There, the velocity of propagation increases with ϵ_r . A difference between different targets on electron density and peak electric field only at a few mm from the surface has also been measured in Klarenaar *et al* (2018a), Sobota *et al* (2019) and simulated in Ji *et al* (2018), Schweigert *et al* (2019b). Finally, the simulation results in figure 6 show the return stroke propagating from the target towards the inner electrode, with both grounded and floating targets. The return stroke propagates faster than the first ionization wave, in agreement with the cases in Darny *et al* (2017), Viegas *et al* (2018a) for grounded target and both positive and negative polarities of applied voltage.

In figure 7, the value of E_{zMAX} along the propagation is presented for the three previously described cases. Both experimental Stark shift measurements and simulation results are shown. In both cases, E_{zMAX} is the peak electric field in the center of the front (Hofmans and Sobota 2019), with a radial uncertainty of the size of the slit width of $100 \mu\text{m}$. As explained in Hofmans and Sobota (2019), E_{zMAX} in the experiments comes from the distance between the allowed and forbidden

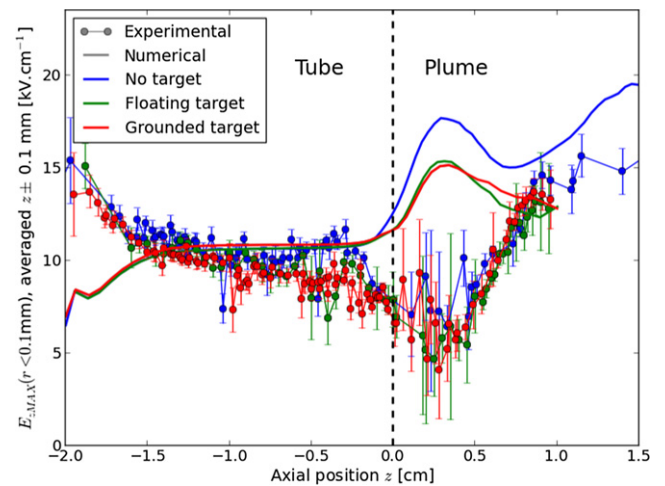


Figure 7. Evolution of the peak electric field along discharge propagation, from simulations and experiments, with $V_P = 5$ kV and for three different configurations: free jet (no target), metallic target at floating potential and grounded. Average within $z \pm 0.1$ mm of E_{zMAX} for $r < 0.1$ mm.

lines of the studied helium band, where the position of the forbidden line changes the most due to the high electric field. The error in the electric field values is taken as the uncertainty of the fit in determining the wavelength position of both lines, yielding values of around $\pm 1 \text{ kV cm}^{-1}$, as can be seen in figure 7. Hence, the measured E_{zMAX} might not be the highest at the measured position, but actually an average value within a range of $\pm 1 \text{ kV cm}^{-1}$. This range of $\pm 1 \text{ kV cm}^{-1}$ around the maximum of E_z corresponds to a distance of around $z \pm 0.1$ mm around its position, according to the simulations. Therefore, we take the average E_z within a distance of $z \pm 0.1$ mm around the maximum of E_z found in the center for $r < 0.1$ mm, accounting for the slit width. The axial averaging of E_z has been shown in Hofmans *et al* (2020) to be a more accurate way to compare simulation results with Stark shift electric field measurements than taking the local maximum of E_z . Moreover, we have verified that the difference between the maximum of E_z for $r < 0.1$ mm and its radial average within $r < 0.1$ mm is negligible.

Between the three different jet configurations, in both experiments and simulations, there are only small differences

in $E_{z\text{MAX}}$. That is also the case for the propagation shown in figure 6 and in the electric field measurements with different targets in Sobota *et al* (2019). $E_{z\text{MAX}}$ obtained from the experiments and from the simulations presents a good agreement, with $E_{z\text{MAX}}$ around 10 kV cm^{-1} in the tube, between $z = -1.5 \text{ cm}$ and $z = -0.5 \text{ cm}$, and rising to higher values ($< 20 \text{ kV cm}^{-1}$) outside the tube. However, as both experiments and simulations assess $E_{z\text{MAX}}$ in the center, the agreement between numerical and experimental results decreases in the regions where the discharge structure is different in experiments and simulations (see figures 4 and 5), as was already the case in Hofmans *et al* (2020) with free jets: close to the electrodes ($z < -1.5 \text{ cm}$) and to the nozzle ($z \simeq 0$). As the experimental discharge is tendentially wider close to the nozzle, the electric field is more off-centered than in the simulations and thus its value at the center is lower in the experiments. Likewise, close to the electrodes, as the discharge is more centered in the experiments, $E_{z\text{MAX}}$ is higher at the center than in the simulations. Moreover, the increase of $E_{z\text{MAX}}$ just outside the tube in the simulations may be due to the change of permittivity between the tube with $\epsilon_r = 4$ and the ambient air with $\epsilon_r = 1$ (Jánský and Bourdon 2011). The fact that the tube edges are sharp in the model, while they are rounded in the experiments, might contribute to the difference. However, as shown in figure 6, the differences between simulations and experiments in discharge structure and $E_{z\text{MAX}}$ do not lead to a significant difference in discharge propagation velocity. Indeed, we have shown in Hofmans *et al* (2020), through comparisons of discharge dynamics with different applied voltages, that $E_{z\text{MAX}}$ profiles are not directly related to discharge propagation velocities, in agreement with studies in air streamer discharges (Babaeva and Naidis 1996). Velocities are dependent on geometry and on the magnitude of applied voltage, while the electric field is related to the local charge separation.

3.2. Jet-target interaction

In this section, we study the dynamics taking place after the impact of the discharge on the target. Firstly, figure 8 presents the temporal evolution of the electric potential in the conductive metallic target at floating potential. Experimental and numerical results are shown for three cases of V_P : 4, 5 and 6 kV. In the experiments, two different lengths of pulse are used for each case: $t_f = 1 \mu\text{s}$ and $t_f = 10 \mu\text{s}$. In the simulations, only $t_f = 1 \mu\text{s}$ is used.

Figure 8 shows that the target potential in the experiments for pulses with $t_f = 10 \mu\text{s}$ starts increasing at the impact of the discharge and slowly rises due to electron emission and ion neutralization until saturation is reached after some μs at a potential slightly below V_P . It is visible that both the time of impact of the discharge and the time of saturation are inversely proportional to V_P . Thus, the pulse width and the applied voltage allow to control the charging of the floating target, as shown also in Slikboer *et al* (2019) for a dielectric target. With short pulses of $t_f = 1 \mu\text{s}$, the charging of the target is interrupted. As the applied voltage in the inner ring electrode is dropped, the target changes from cathode to anode and the electric potential slowly decreases by electron absorption,

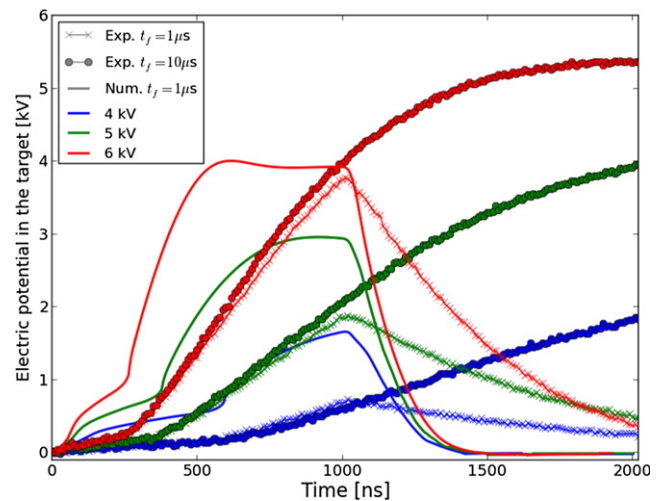


Figure 8. Temporal evolution of the electric potential in the metallic target at floating potential, from simulations and experiments, with $V_P = 4, 5$ and 6 kV .

reaching almost zero at $t = 2 \mu\text{s}$. Negative charge deposition after the fall of the pulse due to reversal of electric field direction has also been observed in experiments and in simulations with different dielectric targets (Viegas *et al* 2018b, Slikboer *et al* 2019, Viegas and Bourdon 2020). However, even with short pulses of $t_f = 1 \mu\text{s}$, the target potential reaches non-negligible values at the end of the pulse, of almost $2/3$ of V_P when $V_P = 6 \text{ kV}$, $1/2$ of V_P when $V_P = 5 \text{ kV}$ and $1/4$ of V_P when $V_P = 4 \text{ kV}$. Conversely, in the simulations the target potential has a first increase with the approach of the discharge, mostly due to electron emission by effect of the electric field. Then, the potential increases faster after the discharge impact. Indeed, it rises faster than in experiments and saturates at about 2 kV below V_P . In the cases with $V_P = 5$ and 6 kV , the saturation takes place during the $1 \mu\text{s}$ pulse, approximately 400 ns after the impact with $V_P = 6 \text{ kV}$ and 600 ns after the impact in the $V_P = 5 \text{ kV}$ case. After the end of the pulse, the potential also decreases faster in simulations than in experiments, decreasing to half its value in about 150 ns , instead of 400 to 700 ns registered in experiments. In both experiments and simulations the rate of charging and uncharging grows with V_P . The difference between the experimental and numerical results of charging of the target will be discussed in section 3.3.

The total charge in the target can also be obtained from the simulations. Although not shown here, it follows approximately the same temporal profile as the electric potential in the target, reaching values of around $2.0, 3.6$ and 4.0 nC at the end of the pulse, respectively, for $V_P = 4, 5$ and 6 kV . These values agree with those presented in Viegas and Bourdon (2020) for $V_P = 6 \text{ kV}$, where it has been shown through simulations that a floating dielectric target of $\epsilon_r = 80$ charges up to 2 nC in about 400 ns and a grounded dielectric target of $\epsilon_r = 56$ charges up to 10 nC in the same timescale. As expected for a floating conductive target, the value obtained here for $V_P = 6 \text{ kV}$ stands between those two cases. However, as the charge is distributed in the large metallic target, 4.0 nC corresponds to only $\sim 0.06 \text{ nC cm}^{-2}$ of surface charge density. This value is much lower than those

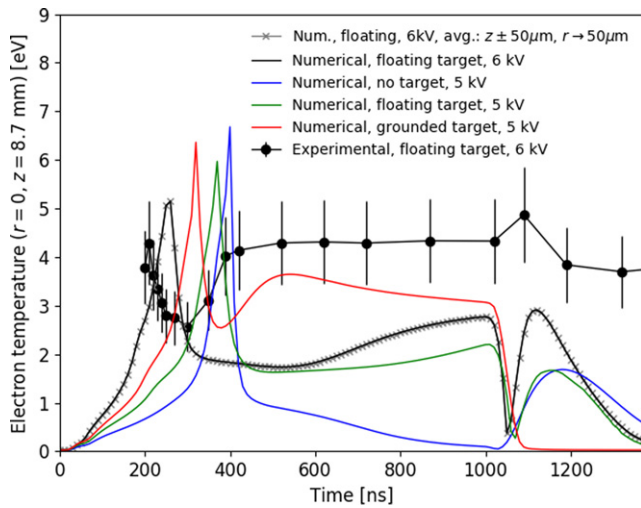


Figure 9. Temporal evolution of the electron temperature at $r = 0$ and $z = 8.7$ mm. From experiments, with metallic target at floating potential and $V_P = 6$ kV. From simulations, with $V_P = 5$ kV and three different configurations and with $V_P = 6$ kV and metallic target at floating potential.

in dielectric targets that charge locally up to 70 nC cm^{-2} (Slikboer *et al* 2019, Viegas and Bourdon 2020). As the target is charged in the model through ion neutralization and electron emission, both driven by the electric field, and considering that electrons are approximately 100 times more mobile than ions, we can conclude that the number of electrons emitted during the charging is of the order of 10^{10} (1 nC corresponding to approximately 6×10^9 elementary charges). Considering the case with $V_P = 6$ kV, where the target charges approximately 1 nC per 100 ns, we can calculate a flux of electron emission through the discharge cross section of $\sim 0.05 \text{ cm}^2$ of approximately $0.2 \text{ nC ns}^{-1} \text{ cm}^{-2}$ or $10^9 \text{ ns}^{-1} \text{ cm}^{-2}$ electrons. Likewise, electrons are absorbed after the fall of the pulse with a flux $\sim 0.3 \text{ nC ns}^{-1} \text{ cm}^{-2}$. Finally, we calculate the self-capacitance of the target as $C = Q/V$ to be between 1.0 and 1.2 pF, where Q is the total charge in the target and V is its potential. In Ito *et al* (2010), with a jet powered by a voltage with peak of 6–7 kV impacting on a copper target with an imposed capacitance in the order of a few pF, the charge accumulated in the target has been measured through time integration of the discharge current to have a maximum of 4 and 5 nC, in agreement with our results.

Despite the differences, both experimental and numerical results in figure 8 support the conclusion that the metallic target at floating potential has a voltage close to zero at the time of discharge impact, which allows it to behave approximately like a grounded target in the instants after the impact. However, at the end of the pulse the target is charged and thus its interaction with the plasma is expected to be different from that of a grounded target. Then, we analyze the consequences of jet-target interaction on the plasma. In the experiments, the temporal evolution of electron temperature T_e and electron density n_e has been measured through Thomson scattering in a jet with $V_P = 6$ kV and floating copper target, in the center at $r = 0$ and at $z = 8.7$ mm, at only 1.3 mm from the target. This is represented in figures 9 and 10.

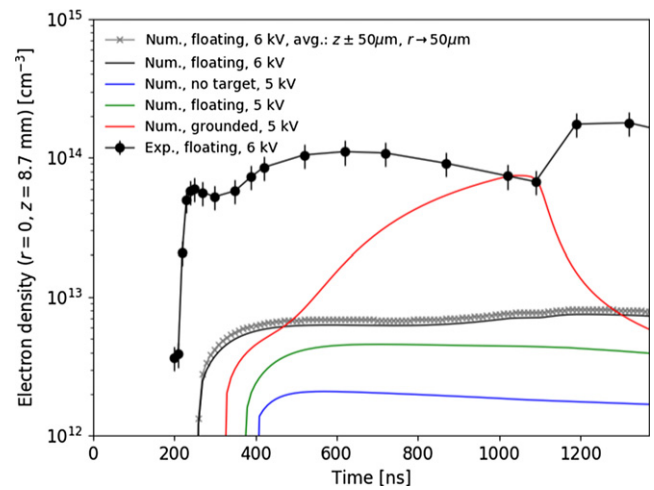


Figure 10. Temporal evolution of the electron density at $r = 0$ and $z = 8.7$ mm. From experiments, with metallic target at floating potential and $V_P = 6$ kV. From simulations, with $V_P = 5$ kV and three different configurations and with $V_P = 6$ kV and metallic target at floating potential.

In the experiments, T_e first increases to 4 eV as the discharge arrives. As the position assessed is very close to the target, the propagation of the return stroke is not distinguishable from this first peak of T_e . Then, as the return stroke propagates further into the tube, T_e decreases close to the target. However, T_e returns to 4 eV and stays with that value until the end of the pulse, which suggests a continuous reactivity in the plume. This would not be the case if the target would charge up to $V_P = 6$ kV, in which case the plasma would tend to be a quasineutral channel. Then, as the applied voltage falls, there is an increase in T_e to almost 5 eV, to which follows a slow decrease. The experimentally-measured n_e follows the same evolution, remaining close to 10^{14} cm^{-3} during the pulse and then increasing after the fall of the pulse. The increase of n_e after the fall of the pulse shows that the electrical redistribution taking place between the inner electrode (now cathode) and the plasma, limited by a target charged at 4 kV (figure 8), can effectively transport or produce a significant amount of electrons. The experimental values of T_e and n_e in this work agree with already published results (Klarenaar *et al* 2018a), where the same jet has been used, but add the increase in n_e after the fall of the pulse.

The experimental T_e and n_e are compared with the simulation results in the same figures (figures 9 and 10) for the same case. The simulation results of T_e and n_e have been retrieved every 10 ns without temporal averaging, as 10 ns is also the duration of each measurement. The numerical results are presented both locally at $r = 0$ and $z = 8.7$ mm and averaged within the volume of the laser beam in the Thomson scattering measurements, i.e. within a cylinder of $50 \mu\text{m}$ radius and $100 \mu\text{m}$ length centered at $r = 0$ and $z = 8.7$ mm. The temporal evolution of the axial component of electric field E_z is also presented, in figure 11, at the same position and in the middle of the plume, at $r = 0$ and $z = 5$ mm. This quantity is not accessible in experiments and therefore is represented exclusively as a simulation result with a resolution of 1 ns.

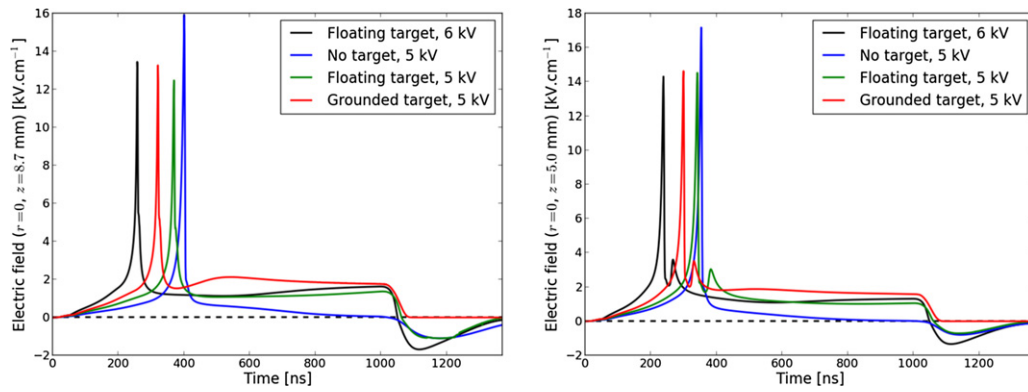


Figure 11. Temporal evolution of the electric field at $r = 0$. On the left, at $z = 8.7$ mm. On the right, at $z = 5.0$ mm. From simulations, with $V_P = 5$ kV and three different configurations and with $V_P = 6$ kV and metallic target at floating potential. The horizontal dashed line signals $E_z = 0$.

The numerical result for the case with floating target and $V_P = 6$ kV (black and grey curves) qualitatively agrees with the experimental measurements. Firstly, the comparison of the two numerical curves of T_e and n_e allows to conclude that although the averaging affects n_e by about 20%, its effect is invisible on T_e and it is not a fundamental factor when analysing the data in this case, due to the relatively small volume of the laser beam. T_e has a peak as the discharge front impacts the target, within the errorbar of the experimental one. The peak takes place 40 ns later than in the experiments due to the difference in time of impact. Then, T_e falls to 2 eV and increases slowly during the pulse until 3 eV. At the end of the pulse, the numerical T_e has a sudden drop and a sudden increase. Although the drop is not obtained by the measurements, the increase is in agreement between simulations and experiments. The numerical values of T_e are generally lower than the experimental ones. We should notice that T_e is obtained from Thomson scattering measurements assuming that the lowest energy electrons (most of the population) follow a Boltzmann EEDF. However, the EEDFs calculated from Bolsig+ present deviations from the Boltzmann EEDFs. Indeed, the EEDFs have more populated bulk and less populated tail than the equilibrium solution. Thus, the Boltzmann assumption potentially leads to an overestimation of T_e from Thomson scattering measurements. This effect has been quantified for argon microwave discharges in Ridenti *et al* (2018), leading to differences in T_e up to a factor 4.

For the same case with floating target and $V_P = 6$ kV (black and grey curves), n_e follows approximately the same evolution in simulations and experiments, but is more than one order of magnitude lower in simulations than in experiments. This difference has already been observed in Hofmans *et al* (2020) in a free jet case and is discussed in that paper, along with the values of n_e and T_e in experiments and simulations. In that work we have verified that the difference between simulations and experiments is in agreement with literature and that it is not expected to be due to any perturbation of the studied discharge by the laser used in the experiments. Then, as in Hofmans *et al* (2020), we assume that the difference may be related to the assumption of oxygen instead of air in the model and to the unknown memory effects of discharge repetition.

E_z presented in figure 11 for the floating target case at $z = 8.7$ mm and $z = 5.0$ mm with $V_P = 6$ kV (black curve) confirms the conclusions taken from the analysis of the temporal evolution of T_e . In addition, figure 11 allows to observe the direction of the electric field at each stage. Firstly, we observe the peak of E_z in the direction of propagation with amplitude 14 kV cm^{-1} associated to the arrival of the discharge front. Then, the return stroke propagates from the target towards the powered electrode as a wave of opposite polarity, with a second peak of E_z that is also positive, as shown in Darny *et al* (2017), Viegas *et al* (2018a). At $z = 8.7$ mm, at only 1.3 mm from the target, the second peak of E_z is very close in time to the first peak and thus is not identifiable. At $z = 5$ mm, the return stroke is associated with a peak of E_z of $\sim 4 \text{ kV cm}^{-1}$. During the rest of the pulse, the electric field in the plasma remains directed downwards with a much lower amplitude close to 1 kV cm^{-1} . After the fall of the applied voltage, E_z reverses sign and then is directed from the charged target towards the inner grounded electrode and tends to neutralize the net charge in the plasma. The reversal of direction causes E_z to pass by zero, which explains the drop of T_e around $t = 1050$ ns in figure 9. Then, E_z has a peak at $t = 1100$ ns in both axial positions of around -2 kV cm^{-1} , which results in a small increase in n_e . The similar peak of E_z in both positions shows that the electrical redistribution at the end of the pulse has a diffusive character and not that of a wave, as suggested by the observations of faint emission in Yue *et al* (2018), Klarenaar *et al* (2018a). Its direction and value below 6 kV cm^{-1} agree with the findings in Lu *et al* (2017).

Besides the cases already discussed, the numerical temporal evolutions of T_e , n_e and E_z are represented in figures 9–11, respectively, for three different jet configurations with $V_P = 5$ kV: free jet, jet with floating target and jet with grounded target. The results for these cases are represented only locally, and not averaged. The simulation results for floating target and $V_P = 5$ kV are very similar to those with $V_P = 6$ kV. Nevertheless, these are significantly different from the results with free jet and with grounded target. For all the cases, the peak T_e and E_z at the arrival of the discharge front at $z = 8.7$ mm stand between 5 and 7 eV and between 12 and 16 kV cm^{-1} , respectively. Then, with free jet, as there is

no return stroke and a quasineutral plasma is formed behind the discharge front, T_e and E_z decrease to low values close to zero after the propagation, in agreement with the experimental observation in Klarenaar *et al* (2018a). n_e in the channel is lower in free jet than with metallic targets, also in agreement with Klarenaar *et al* (2018a). As figures 7 and 11 show that the peak electric field during discharge propagation is not lower in the case without target, we attribute the lower n_e to the absence of the target and of the return stroke. The influence of the return stroke on the increase of n_e has been demonstrated experimentally in Klarenaar *et al* (2018a) and numerically in Viegas (2018), supported by the measurements of helium metastable density in Darny *et al* (2017), and in Yan and Economou (2016).

Here we assess the origin of the increase of n_e during the return stroke. Figure 10 shows that n_e in the plume at $z = 8.7$ mm obtained from the simulations for the case with $V_P = 5$ kV and floating target reaches a value around $2 \times 10^{12} \text{ cm}^{-3}$ higher than in the case without target and thus without return stroke. This increase takes place mostly in the first 100 ns after the impact of the discharge on the target at around $t = 370$ ns. On the one hand, figure 5 shows that the electron-impact ionization source term S_e during those 100 ns does not exceed $10^{17} \text{ cm}^{-3} \text{ s}^{-1}$ and thus cannot produce more n_e than 10^{10} cm^{-3} . Even though other ionization processes take place in volume (Penning ionization, photoionization, associative ionization (Viegas 2018)), they cannot justify an increase in n_e of the order of 10^{12} cm^{-3} . On the other hand, figure 8 shows that the potential of the target rises up to 1.5 kV until $t = 470$ ns, corresponding to a charging of approximately 2 nC and thus the emission of 1.2×10^{10} electrons. If these were homogeneously distributed through diffusive and convective transport in the plasma with 3.8 cm length and 0.125 cm radius (volume 0.19 cm^3), an increase in n_e of $6.4 \times 10^{10} \text{ cm}^{-3}$ (approximately one third of $2 \times 10^{12} \text{ cm}^{-3}$) could be expected. This distribution is not homogeneous in the whole volume and thus the electron emission has a larger impact close to the target, where n_e has been assessed. These results allow to conclude that electron emission from the target and the subsequent transport of electrons in the plasma are the main source of the experimentally and numerically observed increase of n_e and are important aspects of the return stroke.

With grounded target, as a sharp potential gradient remains in the plasma during the pulse, a conductive channel is formed between the electrodes (with the possibility of a transition to an arc phase on longer timescales). T_e and E_z remain relatively high during the pulse, close to 3.5 eV and to 2 kV cm^{-1} , respectively, and n_e increases with time during the pulse up to $8 \times 10^{13} \text{ cm}^{-3}$. This increase in n_e is also associated with electron emission from the target, since S_e presented in figure 5 could only account for an increase in n_e of the order of 10^{11} cm^{-3} in a few hundreds ns. In agreement, Babaeva *et al* (2019) have also reported higher E_z and n_e after discharge impact with grounded target than with floating target. This can explain the higher species production, higher *E. coli* cell inactivation and lower cancer cell viability with grounded targets reported in Ji *et al* (2018), Yue *et al* (2018), Schweigert *et al* (2019a). The difference between targets during the pulse is also visible

in the experimental results of conductive current at the inner ring with $V_P = 5$ kV, presented in figure 2. Indeed, by integrating I_{con} in time, we have measured 6.0 nC in the case with grounded target during the pulse, excluding the positive and negative peaks. Conversely, only 1.1 nC and 1.9 nC have been measured with free jet and with floating target, respectively. These values agree in order of magnitude with the 3.6 nC simulated at the floating target (figure 8).

Then, as the applied voltage falls, the electrical redistribution between the inner ring and the plasma affects the plasma differently in each case. As in the case with floating target with $V_P = 5$ kV, the fall of the pulse in the free jet brings a rise in T_e up to 2 eV and in negative E_z up to -1 kV cm^{-1} , which results in approximately constant n_e . The electric field in these cases is directed from the plasma at positive potential towards the inner grounded ring. Conversely, with grounded target, the electrical redistribution takes place between a grounded inner electrode and a grounded plane. For that reason, its effects are weaker than in the case of a floating target charged at 3 kV in the $V_P = 5$ kV case. Indeed, with grounded target, T_e and E_z decrease to very low values after the pulse and n_e decreases in time. With grounded target, as $E_z \simeq 0$, transport through electric drift is excluded and thus the decrease in n_e after the pulse is attributed to diffusive and chemical losses. As such, we can conclude that in the other two jet configurations n_e is kept constant or increases (with floating target and $V_P = 6$ kV) after the fall of the pulse due to electron emission from the inner electrode and electron transport towards the target. This analysis is reinforced by the negligible values of S_e in the plasma plume after the fall of the pulse observed in figure 5 and by the decrease in electric potential of the target due to electron absorption observed in figure 8. In Kim *et al* (2018) the secondary ionization at the falling edge of a pulse of applied voltage is also claimed to be induced by charge transport. These results concerning the fall of the pulse constitute a major difference between grounding and not grounding the target.

3.3. Discussion on the discrepancy of charging and uncharging the floating metallic target

The faster charging and uncharging of the floating metallic target in simulations than in experiments (figure 8) leads to questioning the conditions for comparison and the assumptions taken in the model. Firstly, both experiments and simulations have verified that changing the position of the grounded plate behind the target between $z = 15$ and $z = 31$ cm has no influence on the results. Then, we should consider that in Slikboer *et al* (2019) we have used the same model with secondary electron emission ($\gamma = 0.1$) instead of a perfect electron emitter assumption to describe the interaction between the discharge and a dielectric BSO target. We have found an excellent agreement with experiments on the electric field evolution inside the target, which is closely related to surface charge, for both charging (ion neutralization and electron emission) and uncharging (electron absorption) of the target. However, taking the same secondary electron emission assumption as in Slikboer *et al* (2019) for the metallic targets has a negligible effect (~ 0.2 kV) on the results of figure 8, although it removes the

potential increase before the discharge impact. Furthermore, it decreases the agreement with experiments in figures 9 and 10.

The model describes metallic surfaces as perfect absorbers and perfect emitters of electrons, and thus ignores the cathodic sheath between the plasma and the metallic surface and simplifies the dynamics of charges between the plasma and the surface. In Naidis (1999) a voltage drop of 0.2–0.3 kV in the sheath between air streamers at atmospheric pressure and cathodes has been suggested. This value is too low to justify the different rate of charging in figure 8. However, a recent work (Cernak *et al* 2020) that highlights the importance of streamer-cathode sheaths has shown through numerical simulations a voltage drop of 1.5 kV over 50 μm when a nitrogen streamer at 26.7 kPa approaches a grounded cathode. Cernak *et al* (2020) also suggest that the description of streamer-cathode sheaths lies outside the conditions for validity of both the drift–diffusion approximation used in fluid models and the two-term approximation for solution of the electron Boltzmann equation.

Furthermore, the works of Bronold and co-authors (Bronold *et al* 2018) have initiated a microscopic description of charge transfer across plasma walls leading to the calculation of electron absorption, backscattering and secondary emission coefficients. Other works (Reess and Paillol 1997, Pechereau *et al* 2016, Babaeva *et al* 2019) simulate the fluxes of electron emission from metallic surfaces from ion bombardment, thermionic emission, field emission or photo-emission processes. These factors point to potential improvements of the model that could lead to better agreement between numerical and experimental results in figure 8.

Finally, in the experiment a thin oxide layer is very likely to be formed on the copper surface interacting with the plasma and could be responsible for diminishing the conductivity of the target (Altieri *et al* 2017). As the model supposes the conductivity to be infinite, this could justify the slower rise and fall of electric potential in the experiments.

4. Conclusions

This work has addressed the interaction of kHz μs -pulsed atmospheric pressure He jets with metallic targets through simulations and experiments, focusing on the differences between floating and grounded targets. Three jet configurations have been studied with positive polarity of applied voltage: free jet, jet with metallic target at floating potential and jet with grounded metallic target. The same conditions have been taken in experiments and simulations. Experimentally, the jets have been studied through imaging and Stark polarization spectroscopy peak electric field measurements. In the case with floating copper target, electron properties in the plasma plume have been assessed through Thomson scattering measurements and the temporal evolution of electric potential of the target under plasma exposure has been measured with a high voltage probe. Numerically, an axisymmetric two-dimensional plasma fluid model has been used. A description of the floating metallic plate as an isopotential infinitely conductive surface where ions are neutralized and electrons are emitted and absorbed through effect of the electric field has been proposed.

Experiments and simulations have observed the same discharge dynamics. The discharge propagates faster towards the grounded target than in the other two configurations. With floating target, the discharge only propagates faster with respect to the free jet case in the last 5 mm of propagation. Moreover, experimental and numerical results both show that the peak electric field at the discharge front during the propagation is approximately the same between the three different configurations. With both grounded and floating targets, a return stroke has been observed after discharge impact on the target, as an ionization wave propagating from the target towards the powered electrode in an already ionized channel. With grounded target, reactivity stays in the plasma plume during the 1 μs pulse, while with floating target it severely decreases in a few hundred ns. At the fall of the applied voltage pulse, another electrical redistribution takes place between the now grounded inner electrode and the positive plasma. This has been shown to have higher intensity with floating target than with grounded target.

The explanations for the differences between grounded and floating targets have been found in the temporal evolution of electric potential of the floating target. The discrepancy between simulations and experiments in that temporal evolution has been discussed, taking into account that the model describes metallic surfaces as perfect absorbers and emitters of electrons. A more accurate description of electron absorption, backscattering and emission from the surfaces has been pointed as a potential future improvement of the model. However, both experiments and simulations have shown that the potential of the floating target after discharge impact increases a few kV per μs , depending on the amplitude of applied voltage. Thus, the pulse width and the applied voltage allow to control the charging of the target. After the pulse, the potential decreases at approximately those rates, until approaching zero. As such, during dozens of ns after the impact, the target is close to grounded but, at the end of the 1 μs pulse, it is at a high voltage, potentially more than half of the applied voltage. That explains the similar return stroke with floating and grounded targets. Furthermore, it justifies the decay in reactivity during the pulse with floating target as the target charges and potential gradients in the plasma dissipate. As a result, simulations have shown that the electron temperature and electric field remain high in the plasma with grounded target and the electron density in the plasma plume increases during the pulse with grounded target but not with floating target or without target.

Finally, the charging of the floating target has shown that the redistribution at the end of the pulse takes place between a grounded inner electrode and a plasma limited by a charged surface in the floating target case, while with grounded target it takes place between two grounded electrodes. That justifies the stronger intensity of that redistribution with floating target. Experiments and simulations have shown an increase in electron temperature, magnitude of electric field and electron density in the plume with floating target after the pulse, which is not the case with grounded target. The increases in electron density in the plume after the pulse with floating target, during the return stroke with both floating and grounded targets and

during the whole pulse with grounded target, have been shown to be mostly due to electron emission from metallic surfaces and charge transport in the plasma.

Acknowledgments

MH is financially supported by the Agence Nationale de la Recherche of France, under project number ANR-16-CE06-0005-01. PV has been supported by a French governmental fellowship attributed by the École Doctorale Ondes et Matière. ZB acknowledges support by project LM2018097 funded by the Ministry of Education, Youth and Sports of the Czech Republic. This work has been done partially within the LABEX Plas@par project, and received financial state aid managed by the Agence Nationale de la Recherche (ANR), as part of the programme 'Investissements d'avenir' under the reference ANR-11-IDEX-0004-02. Simulations presented in this work have been performed thanks to the computational resources of the cluster 'Hopper' at École Polytechnique.

ORCID iDs

Pedro Viegas  <https://orcid.org/0000-0002-3820-3300>
 Marlous Hofmans  <https://orcid.org/0000-0002-8445-5349>
 Adam Obrusník  <https://orcid.org/0000-0002-8415-4909>
 Bart L M Klarenaar  <https://orcid.org/0000-0003-1544-8011>
 Zdenek Bonaventura  <https://orcid.org/0000-0002-9591-6040>
 Olivier Guaitella  <https://orcid.org/0000-0002-6509-6934>
 Ana Sobota  <https://orcid.org/0000-0003-1036-4513>
 Anne Bourdon  <https://orcid.org/0000-0003-3662-4651>

REFERENCES

- Altieri N D, Chen J K-C, Minardi L and Chang J P 2017 *J. Vac. Sci. Technol. A* **35** 05C203
- Arjunan K P, Obrusník A, Jones B T, Zajickova L and Ptasinka S 2016 *Plasma Process. Polym.* **13** 1089–105
- Babaeva N Y and Naidis G 1996 *J. Phys. D: Appl. Phys.* **29** 2423
- Babaeva N Y, Naidis G V, Panov V A, Wang R, Zhang S, Zhang C and Shao T 2019 *Plasma Sources Sci. Technol.* **28** 095006
- Bornholdt S, Wolter M and Kersten H 2010 *Eur. Phys. J. Appl. Phys.* **60** 653–60
- Boselli M, Colombo V, Ghedini E, Gherardi M, Laurita R, Liguori A, Sanibondi P and Stancampiano A 2014 *Plasma Chem. Plasma Process.* **34** 853–69
- Bourdon A, Darny T, Pechereau F, Pouvesle J, Viegas P, Iséni S and Robert E 2016 *Plasma Sources Sci. Technol.* **25** 035002
- Breden D and Raja L L 2014 *Plasma Sources Sci. Technol.* **23** 065020
- Bronold F X, Fehske H, Pamperin M and Thiessen E 2018 *Eur. Phys. J. D* **72** 88
- Cernak M, Hoder T and Bonaventura Z 2020 *Plasma Sources Sci. Technol.* **29** 013001
- Cheng C, Liye Z and Zhan R-J 2006 *Surf. Coat. Technol.* **200** 6659–65
- Collet G, Robert E, Lenoir A, Vandamme M, Darny T, Dozias S, Kieda C and Pouvesle J M 2014 *Plasma Sources Sci. Technol.* **23** 012005
- COMSOL 2016 CFD module user's guide, version 5.3 www.comsol.com/cfd-module
- Darny T, Pouvesle J, Puech V, Douat C, Dozias S and Robert E 2017 *Plasma Sources Sci. Technol.* **26** 045008
- Fanelli F and Fracassi F 2017 *Surf. Coat. Technol.* **322** 174–201
- Fridman G, Friedman G, Gutsol A, Shekhter A B, Vasilets V N and Fridman A 2008 *Plasma Process. Polym.* **5** 503–33
- Graves D B 2014 *Phys. Plasmas* **21** 080901
- Guaitella O and Sobota A 2015 *J. Phys. D: Appl. Phys.* **48** 255202
- Guaitella O, Thevenet F, Guillard C and Rousseau A 2006 *J. Phys. D: Appl. Phys.* **39** 2964–72
- Hagelaar G and Pitchford L 2005 *Plasma Sources Sci. Technol.* **14** 722
- Hofmann S, van Gils K, van der Linden S, Iseni S and Bruggeman P 2014 *Eur. Phys. J. D* **68** 56
- Hofmans M and Sobota A 2019 *J. Appl. Phys.* **125** 043303
- Hofmans M, Viegas P, van Rooij O, Klarenaar B, Guaitella O, Bourdon A and Sobota A 2020 *Plasma Sources Sci. Technol.* **29** 034003
- IST 2018 IST-Lisbon database www.lxcat.net, retrieved on January 2018
- Ito M, Oh J-S, Ohta T, Shiratani M and Hori M 2018 *Plasma Process. Polym.* **15** 1700073
- Ito Y, Fukui Y, Urabe K, Sakai O and Tachibana K 2010 *Japan J. Appl. Phys.* **49** 066201
- Jánký J and Bourdon A 2011 *Appl. Phys. Lett.* **99** 161504
- Ji L, Yan W, Xia Y and Liu D 2018 *J. Appl. Phys.* **123** 183302
- Kim H Y, Golkowski M, Golkowski C, Stoltz P, Cohen M B and Walker M 2018 *Plasma Sources Sci. Technol.* **27** 055011
- Klarenaar B, Guaitella O, Engeln R and Sobota A 2018a *Plasma Sources Sci. Technol.* **27** 085004
- Klarenaar B L M, Brehmer F, Welzel S, van der Meiden H J, van de Sanden M C M and Engeln R 2015 *Rev. Sci. Instrum.* **86** 046106
- Klarenaar B L M, Grofulović M, Morillo-Candas A S, van den Bekerom D C M, Damen M A, van de Sanden M C M, Guaitella O and Engeln R 2018b *Plasma Sources Sci. Technol.* **27** 045009
- Koné A, Sainct F P, Muja C, Caillier B and Guillot P 2017 *Plasma Med.* **7** 333–46
- Kong M G, Kroesen G, Morfill G, Nosenko T, Shimizu T, van Dijk J and Zimmermann J L 2009 *New J. Phys.* **11** 115012
- Laimer J and Stori H 2007 *Plasma Process. Polym.* **4** 266–74
- Laroussi M 2015 *IEEE Trans. Plasma Sci.* **43** 703–12
- Laroussi M and Akan T 2007 *Plasma Process. Polym.* **4** 777–88
- Lazarou C, Anastassiou C, Topala I, Chiper A S, Mihaila I, Pohoata V and Georghiou G E 2018 *Plasma Sources Sci. Technol.* **27** 105007
- Lietz A M, Damany X, Robert E, Pouvesle J-M and Kushner M J 2019 *Plasma Sources Sci. Technol.* **28** 125009
- Lindsay A, Byrns B, King W, Andhvarapou A, Fields J, Knappe D, Fonteno W and Shannon S 2014 *Plasma Chem. Plasma Process.* **34** 1271–90
- Liu Z, Liu D, Xu D, Cai H, Xia W, Wang B, Li Q and Kong M G 2017 *J. Phys. D: Appl. Phys.* **50** 195203
- Loeb L B 1965 *Electrical Coronas* (Berkeley, CA: University of California Press)
- Lu X, Laroussi M and Puech V 2012 *Plasma Sources Sci. Technol.* **21** 034005
- Lu X, Naidis G V, Laroussi M and Ostrikov K 2014 *Phys. Rep.* **540** 123–66
- Lu Y, Wu S, Cheng W and Lu X 2017 *Eur. Phys. J. Spec. Top.* **226** 2979–89
- Martinez L, Dhruv A, Lin L, Balaras E and Keidar M 2019 *Plasma Sources Sci. Technol.* **28** 115002
- Naidis G 1999 *J. Phys. D: Appl. Phys.* **32** 2649–54
- Naidis G V 2011 *J. Phys. D: Appl. Phys.* **44** 215203
- Neys E C 2016 *Plasma Chem. Plasma Process.* **36** 185–212

- Noeske M, Degenhardt J, Strudthoff S and Lommatzsch U 2004 *Int. J. Adhes. Adhes.* **24** 171–7
- Norberg S, Johnsen E and Kushner M 2015 *J. Appl. Phys.* **118** 013301
- Pancheshnyi S, Biagi S, Bordage M, Hagelaar G, Morgan W, Phelps A and Pitchford L 2012 *Chem. Phys.* **398** 148
- Pechereau F, Bonaventura Z and Bourdon A 2016 *Plasma Sources Sci. Technol.* **25** 044004
- Raizer Y P 1991 *Gas Discharge Physics* (Berlin: Springer)
- Reess T and Païllol J 1997 *J. Phys. D: Appl. Phys.* **30** 3115
- Reuter S, von Woedtke T and Weltmann K-D 2018 *J. Phys. D: Appl. Phys.* **51** 233001
- Ridenti M A, de Amorim J, Pino A D, Guerra V and Petrov G 2018 *Phys. Rev. E* **97** 013201
- Robert E, Darny T, Dozias S, Iseni S and Pouvesle J M 2015 *Phys. Plasmas* **22** 122007
- Sakiyama Y, Graves D B and Stoffels E 2008 *J. Phys. D: Appl. Phys.* **41** 095204
- Schutze A, Jeong J Y, Babayan S E, Park J, Selwyn G S and Hicks R F 1998 *IEEE Trans. Plasma Sci.* **26** 1685–94
- Schweigert I, Zakrevsky D, Gugin P, Yelak E, Golubitskaya E, Troitskaya O and Koval O 2019a *Appl. Sci.* **9** 4528
- Schweigert I V, Vagapov S, Lin L and Keidar M 2019b *J. Phys. D: Appl. Phys.* **52** 295201
- Sigmond R 1984 *J. Appl. Phys.* **56** 1355–70
- Simoncelli E, Stancampiano A, Boselli M, Gherardi M and Colombo V 2019 *Plasma* **2** 369–79
- Slikboer E, Guaitella O and Sobota A 2016 *Plasma Sources Sci. Technol.* **25** 03LT04
- Slikboer E, Garcia-Caurel E, Guaitella O and Sobota A 2017 *Plasma Sources Sci. Technol.* **26** 035002
- Slikboer E, Sobota A, Guaitella O and Garcia-Caurel E 2018a *J. Phys. D: Appl. Phys.* **51** 115203
- Slikboer E, Sobota A, Guaitella O and Garcia-Caurel E 2018b *J. Phys. D: Appl. Phys.* **51** 025204
- Slikboer E, Viegas P, Bonaventura Z, Garcia-Caurel E, Sobota A, Bourdon A and Guaitella O 2019 *Plasma Sources Sci. Technol.* **28** 095016
- Sobota A, Guaitella O and Garcia-Caurel E 2013 *J. Phys. D: Appl. Phys.* **46** 372001
- Sobota A et al 2016 *Plasma Sources Sci. Technol.* **25** 065026
- Sobota A, Guaitella O, Sretenovic G B, Kovacevic V V, Slikboer E, Krstic I B, Obradovic B M and Kuraica M M 2019 *Plasma Sources Sci. Technol.* **28** 045003
- Urabe K, Morita T, Tachibana K and Ganguly B N 2010 *J. Phys. D: Appl. Phys.* **43** 095201
- Viegas P 2018 Electric field characterization of atmospheric pressure helium plasma jets through numerical simulations and comparisons with experiments *PhD Thesis* École Polytechnique, France <http://www.theses.fr/2018SACLX061>
- Viegas P and Bourdon A 2020 *Plasma Chem. Plasma Process.* **40** 661–83
- Viegas P, Pechereau F and Bourdon A 2018a *Plasma Sources Sci. Technol.* **27** 025007
- Viegas P, Slikboer E, Obrusník A, Bonaventura Z, Sobota A, Garcia-Caurel E, Guaitella O and Bourdon A 2018b *Plasma Sources Sci. Technol.* **27** 094003
- Wang L, Zheng Y and Jia S 2016 *Phys. Plasmas* **23** 103504
- Wang R, Xu H, Zhao Y, Zhu W, Ostrikov K and Shao T 2019 *J. Phys. D: Appl. Phys.* **52** 074002
- Weltmann K-D and von Woedtke T 2017 *Plasma Phys. Control. Fusion* **59** 014031
- Wild R, Gerling T, Bussiahn R, Weltmann K-D and Stollenwerk L 2014 *J. Phys. D: Appl. Phys.* **47** 042001
- Winter J, Brandenburg R and Weltmann K-D 2015 *Plasma Sources Sci. Technol.* **24** 064001
- Yan W and Economou D J 2016 *J. Appl. Phys.* **120** 123304
- Yue Y, Pei X, Gidon D, Wu F, Wu S and Lu X 2018 *Plasma Sources Sci. Technol.* **27** 064001